

# Neutron interferometry as a dark matter detector

A. Capolupo,<sup>1,\*</sup> G. Pisacane,<sup>1,†</sup> A. Quaranta,<sup>2,‡</sup> and P. Böni<sup>3,§</sup>

<sup>1</sup>*Dipartimento di Fisica “E.R. Caianiello”, Università di Salerno,  
and INFN – Gruppo Collegato di Salerno, Via Giovanni Paolo II, 132, 84084 Fisciano (SA), Italy*

<sup>2</sup>*School of Science and Technology, University of Camerino,  
Via Madonna delle Carceri, Camerino, 62032, Italy*

<sup>3</sup>*Technical University of Munich, TUM School of Natural Sciences, Physics Department, 85748 Garching, Germany*

We analyze the possibility of detecting the existence of mirror matter, a possible component of dark matter, through neutron interferometry. We develop an interferometer using bandpass multilayers in reflection and transmission geometry and discuss its advantages and limitations. We demonstrate that our setup can probe a considerable range of neutron-mirror neutron mixing parameters allowing us to show the existence of mirror matter using present day neutron sources based on fission or spallation processes.

- *Introduction:* - The long-standing puzzles of modern physics, among which i) the composition of the dark sector of the universe [1–10], ii) unresolved questions in particle physics, such as the problem of CP violation by the strong interaction, which has not been observed experimentally, although such a violation can occur according to quantum chromodynamics [11–13], iii) the nature and the origin of neutrino masses and mixing [14–26], and iv) a growing number of experimental anomalies [27–33], require an unprecedented degree of interdisciplinarity and a fair amount of physics beyond the standard model (SM) of particles.

Cosmology and particle physics are becoming increasingly intertwined, posing entirely different problems, yet often pointing to shared solutions. It is sufficient to mention the abundance of axions and axion-like particle models that represent viable candidates for dark matter [34–40] and the deep relationship that has been emerging between particle mixing and the dark sector [41–46]. In this context the neutron lifetime puzzle [47–49] represents another emblematic example. The observed discrepancy between bottle and trap experiments may be elegantly resolved with the addition of a dark counterpart of the neutron, the mirror neutron. The latter can influence the lifetime experiments by mixing with the SM neutrons and emerges naturally in certain extensions of the SM, including mirror matter theory [50–56]. In turn, given the extremely weak interactions that the mirror sector has with the SM, it provides an excellent dark matter candidate [52–56].

In this work, building on the conceptual proposal sketched in [48], we present a novel detection mechanism for mirror neutrons, developing the experimental setup and discussing its advantages and limitations in full detail. The experiment is based on cutting-edge techniques in neutron interferometry, employing advanced

neutron beam manipulation, and on a clever arrangement of external perturbations, including magnetic fields and neutron-transparent nuclear matter. While we frame the analysis in the mirror matter scenario for concreteness, thus realizing the ‘dark neutron’ as mirror-neutron, it is understood that all our conclusions apply to the mixing of neutrons with any dark fermion, regardless of the high energy theory from which it originates. We show that our setup can probe a sizable range of mixing parameters, eventually posing stringent bounds on the coupling constants of the parent model (e.g. mirror matter) and enable the detection of mirror matter.

- *Theoretical Background: neutron - mirror neutron mixing:* - We proceed with a basic outline of mirror matter theory and the phenomenological description of neutron - mirror neutron mixing. The ordinary and mirror sectors, constituting two nearly identical copies of each other, are governed by the same gauge symmetry  $G$ , which in the simplest scenario is taken to be the  $SM$  group,  $G = G_{SM} \equiv SU(3)_c \otimes SU(2)_L \otimes U(1)_Y$ , where  $c$  stands for color,  $SU(2)_L$  is the weak isospin group and  $Y$  is the weak hypercharge. Consequently the gauge group of the mirror matter model is  $G \otimes G$ . Therefore, in addition to the standard Higgs doublet  $\phi$ , there is a corresponding mirror Higgs doublet  $\phi'$ . If the mirror symmetry is exact, then the vacuum expectation values of the Higgs fields  $\phi$  and  $\phi'$  are equal to each other:  $\langle \phi \rangle = \langle \phi' \rangle$ . However, the symmetry can be spontaneously broken if the two Higgs fields take on different vacuum expectation values, i. e.  $\langle \phi \rangle \neq \langle \phi' \rangle$ . In this scenario, the masses of the mirror particles will differ from those of their ordinary counterparts and a universal mixing process between ordinary and mirror neutral hadrons can allow for oscillations between the two sectors.

The mixing of neutral hadrons such as neutrons  $n$  with their mirror counterpart  $n'$  is analogous to two-flavor neutrino mixing and admits a formally identical description. The physical ‘flavor’ states  $n, n'$  are related to the mass states  $n_1, n_2$  via  $\begin{pmatrix} n \\ n' \end{pmatrix} = R(\theta) \begin{pmatrix} n_1 \\ n_2 \end{pmatrix}$ , where  $\theta$  is the mixing angle and  $R(\theta)$  is the rotation matrix. For vanishing momentum the evolution equation in

\* capolupo@sa.infn.it

† gpisacane@unisa.it

‡ aniello.quaranta@unicam.it

§ peter.boeni@tum.de

the flavor basis is described by the Schrödinger equation  $i\frac{d}{dt}\begin{pmatrix} n \\ n' \end{pmatrix} = H\begin{pmatrix} n \\ n' \end{pmatrix}$ , with the mass Hamiltonian

$$H = \begin{pmatrix} m_n + \Delta E & \epsilon_{nn'} \\ \epsilon_{nn'} & m_n + \delta m \end{pmatrix}, \quad (1)$$

where  $m_n$  is the neutron mass,  $\epsilon_{nn'}$  is the mixing amplitude,  $\Delta E$  is the energy contributed to the neutron by eventual external potentials, and  $\delta m = m_{n'} - m_n$  is the  $n - n'$  mass splitting that survives in the limit  $\Delta E = 0$ ,  $\epsilon_{nn'} \rightarrow 0$ . Upper bounds on  $\epsilon_{nn'}$  and  $\delta m$  have been obtained in [47] and are  $\delta m \lesssim 10^{-7}\text{eV}$ ,  $\epsilon_{nn'} \lesssim 10^{-9}\text{eV}$ . Diagonalizing the Hamiltonian  $H$ , we obtain the mixing angle:

$$\tan(2\theta) = \frac{2\epsilon_{nn'}}{\delta m - \Delta E}, \quad (2)$$

and the eigenvalues:

$$m_{1,2} = \frac{1}{2} \left( 2m_n + \Delta E + \delta m \mp \sqrt{(\Delta E - \delta m)^2 + 4\epsilon_{nn'}^2} \right). \quad (3)$$

For generic 3-momentum  $\vec{k}$  the relativistic energy for a free particle of mass  $m_j$  is  $\omega_j = \sqrt{m_j^2 + k^2}$  with  $k = |\vec{k}|$ . Then the eigenstates of  $H$ , including kinetic energy,

evolve according to  $|n_j(t)\rangle = e^{-i\omega_j t} |n_j\rangle$ , where  $|n_j\rangle = |n_j(t=0)\rangle$ .

- *Experimental setup:* - In order to reveal the existence of mirror neutrons, and to measure the mass difference between the neutrons and the mirror-neutrons, we propose using a Mach-Zehnder-type neutron interferometer as sketched in Fig. 1 and proposed by Ebisawa et al. [60]. We employ half-transparent bandpass multilayers for the beam splitter (BS) and the recombining mirror (REC) (Fig. 1) [66]. The bandpass mirrors  $C_I$  and  $C_{II}$  reflect the neutrons onto REC where the beams interfere. The intensity of the reflected and transmitted beams are recorded with detectors O and H, respectively.

The angle of reflection of the neutrons at the mirror positions in degrees is given by  $\theta_c = 0.099m\lambda$ , where  $m$  is defined to be 1 for a Ni coating and  $\lambda$  designates the wavelength of the neutrons in units of  $\text{\AA}$  [65]. Current supermirror technology enables  $m$ -values of the order of  $m \simeq 8$  if the number of supermirror layers is increased to approximately  $N \simeq 16000$  [64]. To achieve a reasonably large beam separation of the order of 80 mm at  $C_I$  and  $C_{II}$ , we propose the use of neutrons with  $\lambda = 8 \text{\AA}$  and supermirror with  $m = 6$ . This choice results in reflection angles of  $\theta_c \simeq 4.8^\circ$  for flight paths of 500 mm between the BS and the REC mirrors and the reflection mirrors, respectively.

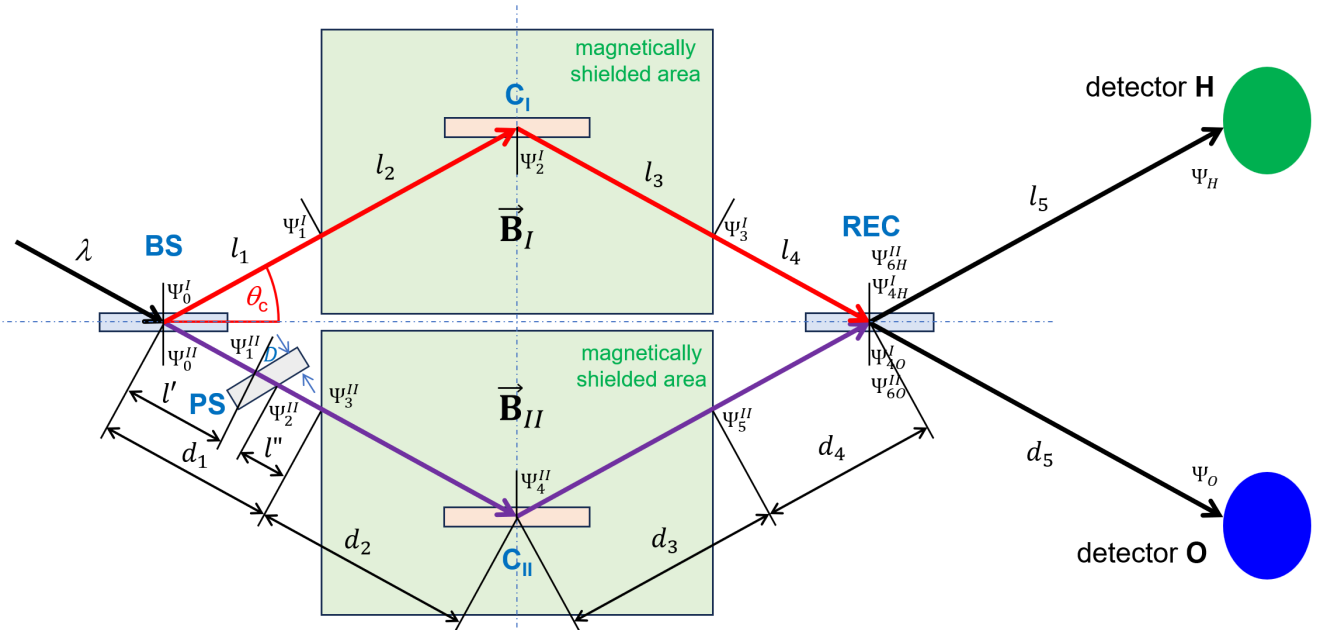


FIG. 1. Scheme of the neutron interferometer, with path I (red arrows) and path II (violet arrows). The regions in green are magnetically shielded against disturbing external fields by mu-metal. The incident polarized beam is split by the beam splitter BS in two beams and after their respective reflection from mirrors  $C_I$  and  $C_{II}$  recombined in the recombination mirror REC. The transmitted and reflected beam thereof are measured with detectors O and H. By rotating the phase shifter PS about the vertical axis and adjusting the amplitude of the magnetic field  $\vec{B}_{II}$ , the phase of the neutrons along path II can be varied. For more details see the text.

To improve the intensity of the set-up, we propose installing band pass mirrors with a bandwidth  $\delta_B = \Delta\lambda/\lambda \simeq 10\% - 20\%$  centered at  $\lambda = 8 \text{ \AA}$  that is reasonably close to the flux maximum of typical cold sources. These mirrors reflect neutrons with a higher efficiency when compared with supermirror. The appropriate  $\delta_B$  is obtained by coating layers of non-magnetic Ni and Ti that cover an  $m$ -range  $5.7 \leq m \leq 6.3$  of a supermirror sequence [59]. For the reflecting mirrors  $C_I$  and  $C_{II}$ , a layer sequence providing a high reflectivity of the order of 90% will be used while for the BS and REC mirrors, the number of layers per unit interval  $\delta m$  will be reduced such that a reflectivity  $R \simeq 50\%$  and therefore a transmission of  $T \simeq 50\%$  is obtained. The incident beam is polarized by using a polarizing supermirror with an Fe/Si coating  $m = 3$  yielding a reflection angle  $\theta_m \simeq 1.2^\circ$  and a polarization  $P \simeq 99\%$  [64]. Therefore, the incident beam can be directed along the optical axis of the interferometer (horizontal dashed line in Fig. 1) thus simplifying its installation at a beam port.

It is planned to mount both the polarizing and reflecting mirrors with a high accuracy to each other using precisely machined base and cover plates made from glass employing technologies similar to those used for neutron guides. In addition, precision adjustments as implemented in ultrastable laser systems and in optical reference cavities will be employed. This means that the interferometer can be considered a single neutron optical component that requires no adjustment of mirrors.

The BS mirror directs the incident polarized neutron beam to the two arms designated as Path I (red arrows) and Path II (violet arrows) in Fig. 1):

- Path I: The reflected neutron beam travels along a section  $l_1$ , where a magnetic guide field  $B_g = 2 \text{ mT}$  is applied to maintain the polarization. Then it travels along the sections  $l_2$  and  $l_3$ , which are exposed to the magnetic field  $B_I$ , and along sections  $l_4$  and  $l_5$  (or  $d_5$ ), where along  $l_4$  a guide field  $B_g = 2 \text{ mT}$  is applied.

- Path II: The transmitted neutron beam passes first a region, where a guide field  $B_g = 2 \text{ mT}$  is applied. It contains the phase shifter with a thickness  $D$  made from Si and completes the paths  $d_2$  and  $d_3$ , where a magnetic field  $B_{II}$  is applied. Finally the neutrons travel along sections  $d_4$  and  $d_5$  (or  $l_5$ ), where again a guide field  $B_g = 2 \text{ mT}$  is applied along  $d_4$ . The phase shift of the neutrons can be varied by rotation of the Si block.

The magnetic fields  $B_I$  and  $B_{II}$  are assumed to be applied perpendicular to the the neutron flight paths, i. e. perpendicular the scheme shown in Fig. 1 and therefore parallel to the surface of the mirrors. Thus the polarization of the neutrons is always kept parallel to the overall polarization  $\mathbf{P}$  of the neutron beam. Of course, spin flippers could be integrated into the beam paths to enable further manipulation of the neutron beams and their phases. However, these possibilities are not discussed here.

*Geometry.* Let us now specify the geometric details of the setup of Fig. 1: The wavefronts of the beams are

perpendicular to the plane of the interferometer. The angles of incidence and reflection are equal to  $4.8^\circ$  with respect to the line joining the beam splitter BS and the recombination mirror REC (horizontal dashed line in Fig. 1). We choose two different sets of parameters, reported in tables I and II. In the first setup, the flight paths are  $l := l_1 = l_4 = d_1 = d_4 = 200 \text{ mm}$  and  $L := l_2 = l_3 = d_2 = d_3 = 300 \text{ mm}$  yielding an overall path length  $2 \cdot (l + L) \simeq 1000 \text{ mm}$  between BS and REC. In addition, we fix  $d := l_5 = d_5 = 500 \text{ mm}$ .

In the second configuration, the flight path lengths are reduced to one-fifth when compared to those mentioned above, in order to reproduce the characteristic lengths of the interferometer presented in Ref. [60] for which the specifications have been worked out in detail. The flight paths  $l_2$ ,  $l_3$ ,  $d_2$  and  $d_3$  are shielded against external fields (for example the Earth's magnetic field) using mu-metal to ensure a precise definition of the fields along the flight paths [62]. To improve the accuracy of the field configuration, the guide fields  $B_g = 2 \text{ mT}$  before and after the greenish region are also shielded with mu-metal.

*Phase shifter.* A slab of phase shifting material with a thickness  $D$  of refractive material, for example Si, with potential  $V$ , induces a time lag for beams along Path II. For a plane wave traversing the slab, the lag is  $\chi = kD_{eff}(n_r - 1)$  [63], where  $n_r$  is the refraction index given by  $n_r = \frac{K}{k} = \sqrt{1 - \frac{V - V_{air}}{E - V_{air}}}$ ,  $D_{eff}$  is the effective length of the beam path of the neutrons in the slab that depends on the rotation angle of the Si-block and  $V$  is the slab potential  $V = \frac{2\pi\hbar^2 N b_c}{m_n}$ . Here,  $b_c$  is the coherent scattering length,  $N$  the atomic density, and  $m_n$  the neutron mass.  $V_{air}$  is the potential of air that can be neglected in most cases. It depends on temperature, pressure and humidity.

- *Hamiltonian and background elements:* - We first consider, for simplicity, a monochromatic beam of cold neutrons with momentum  $k \ll m_n$  and negligible momentum spread  $\delta_B$ . The discussion for a Gaussian wave packet is reported in appendix C.

Such a beam is well described by a plane wave. For a specific value of  $m_n$ , the kinetic energy is (we set  $\hbar = 1 = c$ ):  $\frac{K^2(V)}{2m_n} = \frac{k^2}{2m_n} (1 - \frac{V}{E}) \simeq \frac{k^2}{2m_n} (1 - \frac{V}{m_n})$ . Here, we have assumed  $V_{air} = 0$  and we have neglected terms of higher order in  $k/m$ . The physical states  $|n\rangle$  and  $|n'\rangle$  evolve according to the mass Hamiltonian  $M(V, B)$ , obtained from  $H$  (Eq. (1)), by setting  $\Delta E = -\mu_n B + V$ , i.e.  $M(V, B) = \begin{pmatrix} m_n - \mu_n B + V & \epsilon_{nn'} \\ \epsilon_{nn'} & m_n + \delta m \end{pmatrix}$ . Note that, in path I,  $B = B_g$  along the sections  $l_1$  and  $l_4$ , and  $B = B_I$  along the sections  $l_2$  and  $l_3$ . Moreover, in path II,  $B = B_g$  along  $d_1$  and  $d_4$ , and  $B = B_{II}$  along  $d_2$  and  $d_3$ , (see Fig. 1).

<sup>1</sup> The relation  $k \ll m_n$  is to be understood in natural units ( $c = \hbar = 1$ ):  $\hbar k \ll m_n c$ .

The full Hamiltonian, comprising the kinetic term, is  $H(V, B) = M(V, B) + \frac{k^2}{2M(V, B)} \left(1 - \frac{V}{M(V, B)}\right)$ , where the slight abuse of notation  $1/M$  is to be understood in terms of the eigenvalues of  $M$ . We introduce the mixing angle  $\theta(V, B) = \frac{1}{2} \arctan \left( \frac{2\epsilon_{nn'}}{\delta m + \mu_n B - V} \right)$ , the eigenstates  $|n_1(V, B)\rangle, |n_2(V, B)\rangle$ , and the corresponding eigenvalues

$$\Omega_{1,2}(V, B) = \frac{1}{2} \left( 2m_n + \delta m - \mu_n B \pm \sqrt{(\delta m + \mu_n B - V)^2 + 4\epsilon_{nn'}^2} \right), \quad (4)$$

and we set  $E_{1,2}(V, B) = \Omega_{1,2}(V, B) + \frac{k^2}{2\Omega_{1,2}(V, B)} \left(1 - \frac{V}{\Omega_{1,2}(V, B)}\right)$  for the eigenvalues of the complete Hamiltonian. The neutron-mirror basis is related to the eigenstates  $|n_1(V, B)\rangle$  and  $|n_2(V, B)\rangle$  through

$$\begin{aligned} |n\rangle &= \cos \theta(V, B) |n_1(V, B)\rangle + \sin \theta(V, B) |n_2(V, B)\rangle \\ |n'\rangle &= -\sin \theta(V, B) |n_1(V, B)\rangle + \cos \theta(V, B) |n_2(V, B)\rangle. \end{aligned} \quad (5)$$

The group velocity is defined for each of the eigenvalues as  $v_{1,2}(V, B) = \frac{K(V)}{\Omega_{1,2}(V, B)}$ . If the neutron had a definite mass (no mixing), we would expect a group velocity  $v = v_n(V) \simeq \frac{K(V)}{m_n}$ . The difference among all these velocities is however negligible<sup>2</sup>. Therefore, we consider a single velocity in the beam given by  $v = v_n(V)$ .

The last elements impacting the beam propagation are the mirrors, which are characterized by a transmission and reflection coefficient  $T$  and  $R$ , respectively, related to the neutron fraction which is transmitted  $|T|^2$  and reflected  $|R|^2$ . We assume that the mirrors are fully transparent for the mirror neutron component. For the central mirrors  $J = C_I, C_{II}$  we adopt the following parametrization for the reflection and transmission coefficients  $R_J = \cos \Gamma_J e^{-i\phi_{RJ}}$ , and  $T_J = \sin \Gamma_J e^{-i\phi_{TJ}}$ , since  $|R|^2 + |T|^2 = 1$  must always hold. Note that since only the reflected part from the central mirrors is relevant to the final output, any neutron absorption by  $C_I$  and  $C_{II}$  can be included in the transmission coefficient  $T_J$ . The situation is different for the  $REC$  mirror, for which both reflected and transmitted amplitudes play a role in the final output. Here, neutron absorption must be explicitly taken into account. Letting  $A_{REC}$  denote the fractional intensity absorbed by  $REC$  and setting  $R_{REC} =$

$\cos \Gamma_{REC} e^{-i\phi_{R_{REC}}}$ ,  $T_{REC} = \sin \Gamma_{REC} e^{-i\phi_{T_{REC}}}$ , the reflected and transmitted amplitudes are proportional respectively to  $\sqrt{1 - A_{REC}} R_{REC}$  and  $\sqrt{1 - A_{REC}} T_{REC}$ . The effect of the beam splitter BS is instead included in the initial neutron amplitudes. The exact values of  $\Gamma_J$ ,  $\phi_{RJ}$  and  $\phi_{TJ}$  depend on the specifics of the mirrors used.

- *Propagation of the beam:* - We now have all the elements needed to describe the evolution of the beams along paths I and II. At each step, we express the state of the beam on the neutron - mirror neutron basis, as

$$|\psi^J(t)\rangle = N^J(t) |n\rangle + M^J(t) |n'\rangle, \quad (6)$$

where  $N^J(t)$  and  $M^J(t)$  are the amplitudes for the neutron and the mirror-neutron respectively.

- *Beam I:* We assume that the neutron beam impinges the beam splitter at  $t = 0$ . It is comprised only of a neutron component because the mirror part is not reflected by the polarizer. Let  $N_0^I$  and  $N_0^{II}$  denote the initial amplitudes for beam I and II (see appendix A).<sup>3</sup> The initial state for beam I is therefore  $|\psi^I(0)\rangle = N_0^I |n\rangle$ . The beam traverses a region with a small guide field of 2 mT of length  $l_1 = l$ . One has the normalized state reported in appendix A. Then it traverses the area filled with magnetic field  $B_I$  for a distance  $l_2 = L$ , up to the central mirror  $C_I$ . The state at the entrance of the magnetic area has the form  $|\psi_1^I\rangle = N_1^I |n\rangle + M_1^I |n'\rangle$ . Since the mirror neutron component is entirely transmitted through the mirror  $C_I$ , the state after reflection from  $C_I$  is just  $|\psi_2^I\rangle = R_C^I N_2^I |n\rangle$  with  $N_2^I$  being an appropriate combination of  $N_1^I$  and  $M_1^I$  (see also appendix A).

We now iterate the same process for another length  $L$ . At the exit of the magnetic area, the state is  $|\psi_3^I\rangle = N_3^I |n\rangle + M_3^I |n'\rangle$ . The beam traverses another field region with 2 mT of a length  $l_4 = l$ , thus, after the recombination mirror, one has  $|\psi_{4H}^I\rangle = \sqrt{1 - A_{REC}} R_{REC} N_4^I |n\rangle$  and  $|\psi_{4O}^I\rangle = \sqrt{1 - A_{REC}} T_{REC} N_4^I |n\rangle + M_4^I |n'\rangle$ , respectively, directed towards the H and O detector. All the mathematical details and the explicit expressions of the coefficients  $N_j^I$ ,  $M_j^I$ , (with  $j = 0, \dots, 4$ )  $R_C^I$ ,  $R_{REC}$  and  $T_{REC}$  are reported in appendices A and B.

- *Beam II:* The initial state is now given by  $|\psi_0^{II}\rangle = N_0^{II} |n\rangle + M_0 |n'\rangle$ . The presence of a neutron mirror component is due to the lack of interaction between mirror matter and ordinary matter, and therefore with the BS. This results in complete transmission of the mirror part by the devices. Then the beam evolves in a region with a magnetic guide field of intensity 2 mT for a distance  $l'$ . At the entrance of the slab, the state is given by  $|\psi_1^{II}\rangle = N_1^{II} |n\rangle + M_1^{II} |n'\rangle$ . After crossing the slab for length  $D_{eff}$ , the state is  $|\psi_2^{II}\rangle = N_2^{II} |n\rangle + M_2^{II} |n'\rangle$ . Next, the beam traverses a region, with the magnetic guide field of 2 mT, for a length  $l''$ . The wave function at

<sup>2</sup> In fact, one has:

$$K(V) \left( \frac{1}{\Omega_{1,2}(V, B)} - \frac{1}{m_n} \right) = \frac{K(V)}{m_n} \left[ \frac{-\delta m + \mu_n B - V}{2\Omega_{1,2}(V, B)} \pm \frac{\sqrt{(\delta m + \mu_n B - V)^2 + 4\epsilon_{nn'}^2}}{2\Omega_{1,2}(V, B)} \right].$$

The term in brackets goes as  $\frac{\delta E}{m_n}$ , where  $\delta E$  is the sum of various small (compared to  $m_n$  and even to  $k$ ) energy shifts.

<sup>3</sup>  $N_0^I$  and  $N_0^{II}$  include the term  $\sqrt{1 - A_{BS}}$ , with  $A_{BS}$  designating the absorption coefficient in the beam splitter.

the entrance of the shielded region is denoted by  $|\psi_3^{II}\rangle = N_3^{II}|n\rangle + M_3^{II}|n'\rangle$ . Only the neutron part is reflected by the central mirror  $C_{II}$ , so that the state, immediately after  $C_{II}$  is  $|\psi_4^{II}\rangle = R_C^{II}N_4^{II}|n\rangle$ . Subsequently, the beam exits the area with magnetic field  $B_{II}$  with state  $|\psi_5^{II}\rangle = N_5^{II}|n\rangle + M_5^{II}|n'\rangle$  and evolves in a region with 2 mT up to the recombination mirror. After the recombination mirror, one has  $|\psi_{6O}^{II}\rangle = \sqrt{1 - A_{REC}}R_{REC}N_6^{II}|n\rangle$ , and  $|\psi_{6H}^{II}\rangle = \sqrt{1 - A_{REC}}T_{REC}N_6^{II}|n\rangle + M_6^{II}|n'\rangle$ .

Then, the  $H$  and  $O$  beams, directed towards the respective detectors, are described by the following amplitudes:

$$\begin{aligned} |\psi_H^{in}\rangle &= \sqrt{(1 - A_{REC})(T_{REC}N_6^{II} + R_{REC}N_4^I)}|n\rangle + M_6^{II}|n'\rangle \\ |\psi_O^{in}\rangle &= \sqrt{(1 - A_{REC})(T_{REC}N_4^I + R_{REC}N_6^{II})}|n\rangle + M_4^I|n'\rangle. \end{aligned} \quad (7)$$

Finally, both of them evolve in a free region of length  $l_5 = d_5$  before detection. At the detectors, dropping the  $n'$  part, one has  $|\psi_H\rangle = (N_H^I + N_H^{II})|n\rangle$  and  $|\psi_O\rangle = (N_O^I + N_O^{II})|n\rangle$ , thus, the intensities are given by

$$\begin{aligned} I_{O,H} &\propto \langle \psi_{O,H} | \psi_{O,H} \rangle \\ &= |N_{O,H}^I|^2 + |N_{O,H}^{II}|^2 + 2\text{Re}(\bar{N}_{O,H}^I N_{O,H}^{II}), \end{aligned} \quad (8)$$

where we denote with  $\bar{N}$  the complex conjugate of  $N$ . These output intensities are sensitive to the presence of neutron - mirror neutron mixing.

- *Numerical analysis:* - In the light of the parametrization for the reflection and transmission coefficients  $R_J = \cos \Gamma_J e^{-i\phi_{RJ}}$ , and  $T_J = \sin \Gamma_J e^{-i\phi_{TJ}}$ , we set the various parameters as outlined in Appendix B and reported in tables I and II.

Parameters	Value
$\varphi_{T_{BS}} = \varphi_{T_C^I} = \varphi_{T_C^{II}} = \varphi_{T_{REC}}$	0
$\varphi_{R_{BS}} = \varphi_{R_C^I} = \varphi_{R_C^{II}} = \varphi_{R_{REC}}$	$\frac{\pi}{2}$
$L_P$	0.2 m
$l_1 = l_4 = d_1 = d_4 := l$	0.2 m
$l_2 = l_3 = d_2 = d_3 := L$	0.3 m
$l' = l''$	0.09 m
$D$	0.02 m
$l_5 = d_5 := d$	0.5 m
$\lambda$	8 Å
$m$	6.0
$\Gamma_{R_C^{II}} = \Gamma_{R_C^I}$	0.02
$\Gamma_{REC}$	$\frac{\pi}{3}$
$V$	54 neV
$n$	0.99
$\Gamma_{N_0^I} = \Gamma_{N_0^{II}}$	$\frac{\pi}{4}$
$B_I$	0 T
$B_{II}$	$2 \cdot 10^{-2}$ T
$A_{REC}$	0.01
$A_{BS}$	0.01

TABLE I. Parameters of the interferometer in the first configuration. For our simulations, we assume the use of supermirror with  $m = 6.0$ .  $L_P$  denotes the distance between the polarizing mirror and  $BS$ .

Parameters	Value
$\varphi_{T_{BS}} = \varphi_{T_C^I} = \varphi_{T_C^{II}} = \varphi_{T_{REC}}$	0
$\varphi_{R_{BS}} = \varphi_{R_C^I} = \varphi_{R_C^{II}} = \varphi_{R_{REC}}$	$\frac{\pi}{2}$
$L_P$	0.2 m
$l_1 = l_4 = d_1 = d_4 := l$	0.04 m
$l_2 = l_3 = d_2 = d_3 := L$	0.06 m
$l' = l''$	0.018 m
$D$	0.004 m
$l_5 = d_5 = d$	0.1 m
$\lambda$	8 Å
$m$	6.0
$\Gamma_{R_C^{II}} = \Gamma_{R_C^I}$	0.02
$\Gamma_{REC}$	$\frac{\pi}{3}$
$V$	54 neV
$n$	0.99
$\Gamma_{N_0^I} = \Gamma_{N_0^{II}}$	$\frac{\pi}{4}$
$B_I$	0 T
$B_{II}$	$2 \cdot 10^{-2}$ T
$A_{REC}$	0.01
$A_{BS}$	0.01

TABLE II. Parameters of the interferometer in ref. [60]. We assume supermirror  $m = 6.0$ .  $L_P$  denotes the distance between the polarizing mirror and  $BS$ .

Our analysis is based on the experimental setup proposed in Fig. 1 and the parameters given in tables I and II. In the plots presented in the following, in the upper figures we use the parameters of tab. I and in the lower figures we use those of tab. II. In Fig. 2, we plot the normalized intensity (obtained assuming total intensity equal to unity at the beam splitter, in arbitrary units)  $I_O$  as a function of the parameter  $\epsilon_{nn'}$  for fixed values of  $\delta m$ . Above  $\epsilon_{nn'} \simeq 2 \cdot 10^{-10}$  and  $\delta m = 10^{-8}$  eV, clear deviations from the case without mixing are observed. The insets show  $I_O$  as a function of  $\delta m$  for constant values of  $\epsilon_{nn'}$ . For  $\epsilon_{nn'} = 10^{-9}$  eV, clear deviations from the zero-energy case are predicted.

The zero-energy case can be achieved by choosing a reference beam crossing a region in which  $\mu_n B \gg \epsilon_{nn'}, \delta m$ , such that the mixing angles go to zero and the oscillation phenomenon is suppressed. This high field configuration allows for the normalization of the H and O detectors during an experiment. The simulations show that, for the considered values of  $\delta m$  and  $\epsilon_{n,n'}$ , the configuration with the parameters from tab. I is more sensitive for the detection of mirror neutrons. This finding is also confirmed in the following figures, and it is due to the oscillatory behavior of the intensities at the detector given by eqs.(8), as can be seen explicitly by eqs.(B1) - (B9).

Fig. 3 shows the interference term  $I_O^{INT} = 2\text{Re}(\bar{N}_O^I N_O^{II})$  as a function of  $\epsilon_{nn'}$  and  $\delta m$  in terms of a contour plot. The interference term can be measured by subtracting the high field data from the data measured at a field  $\mu_n B \ll \epsilon_{nn'}, \delta m$ . In Figure 4, we plot the difference  $I_H - I_O$  as a function of  $\epsilon_{nn'}$  for  $\delta m$  constant. The insets show  $I_H - I_O$  as a function of  $\delta m$ , for constant  $\epsilon_{nn'}$ . Obviously,  $I_H - I_O$  depends strongly on  $\epsilon_{nn'}$  and

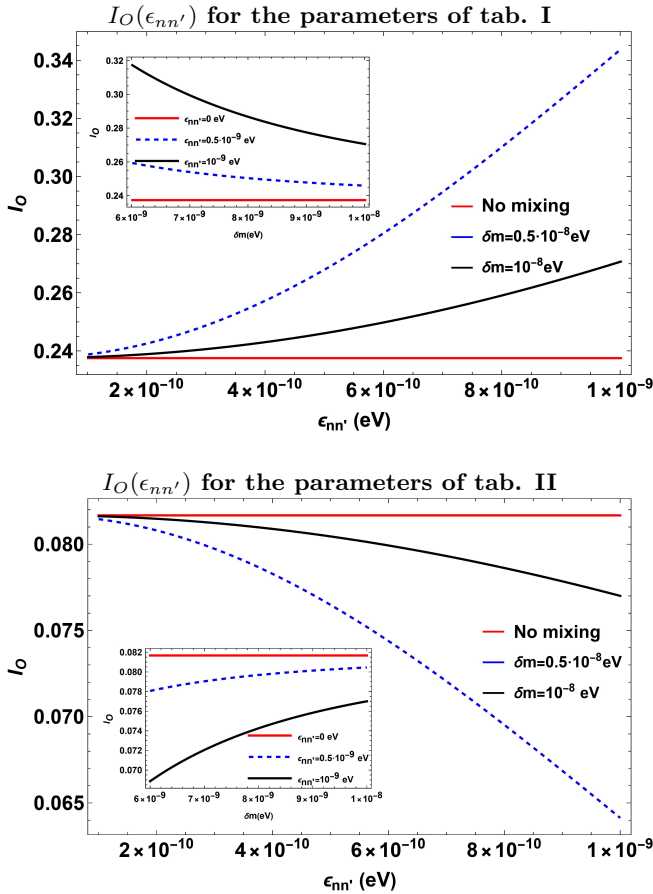


FIG. 2. Plots of the intensity  $I_O$  as a function of  $\epsilon_{nn'} \in [10^{-10}, 10^{-9}]$  eV for fixed values of  $\delta m$ . Red line: case without mixing, blue dotted line:  $\delta m = 0.5 \cdot 10^{-8}$  eV, and black line:  $\delta m = 10^{-8}$  eV. The insets show  $I_O$  as a function of  $\delta m \in [6 \cdot 10^{-9}, 10^{-8}]$  eV, for constant values of  $\epsilon_{nn'}$ ; red line:  $\epsilon_{nn'} = 0$  eV (case without mixing), blue dotted line:  $\epsilon_{nn'} = 0.5 \cdot 10^{-9}$  eV, and black line:  $\epsilon_{nn'} = 10^{-9}$  eV.

$\delta m$ .

Note that for  $\epsilon_{nn'} = 0$ , one has  $\theta = 0$ , the mixing is absent and the difference  $I_H - I_O \neq 0$  and constant, exclusively because of the phase shifter and of the magnetic fields that are different in the two arms. These effects are tiny compared to the intensity difference induced by the mixing, as shown in Fig. 4. On the contrary, the presence of mixing makes this difference, in principle, visible and therefore it can be used to highlight the presence of mirror-neutrons.

We point out that several factors influence the quality and visibility of the experimental outcome:

- The choice of the phases in eqs.(B9), which are determined by the parameters given in tables I and II. They can be adjusted by using different materials for the mirrors and the beam splitter in order to relate the intensity of the detected beam exclusively to the neutron - mirror neutron oscillation. Indeed, the presence of a non-zero exponential phase could alter the intensity of the detected beam due to spurious effects, unrelated to the presence of

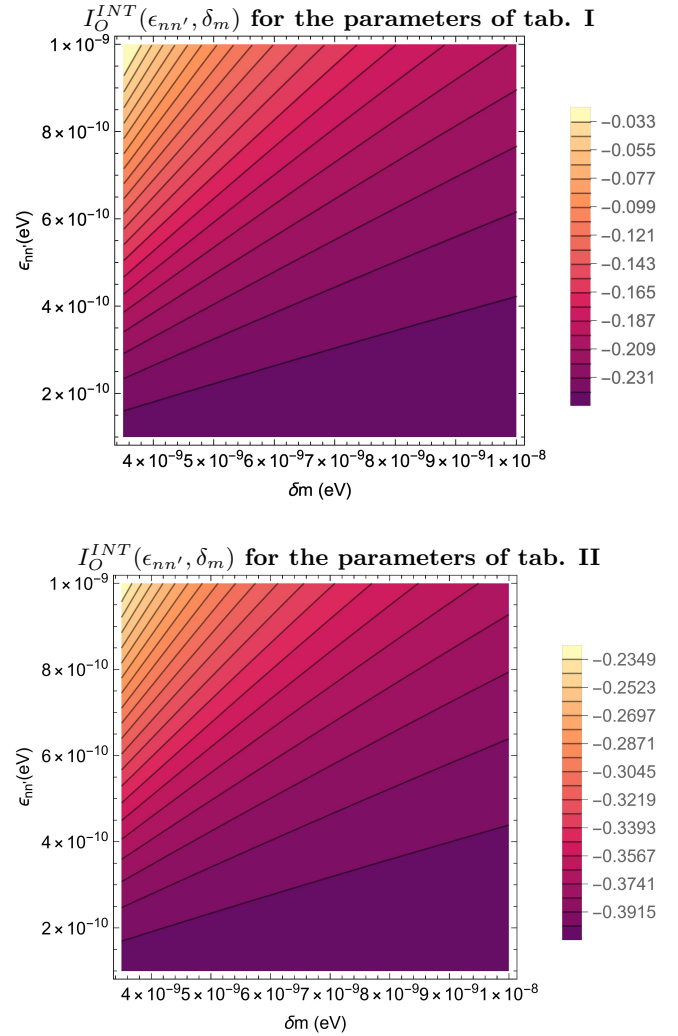


FIG. 3. Contour plots of the interference intensity  $I_O^{INT}$  as a function of  $\epsilon_{nn'} \in [10^{-10}, 10^{-9}]$  eV and  $\delta m \in [3.5 \cdot 10^{-9}, 10^{-8}]$  eV.

mirror neutrons. The best choice for the material is definitely Si, since it has a small absorption, is non-magnetic, and perfect crystals are available. Si is also the preferred material for single crystal interferometers [57].

- The potential (and therefore the material) that characterizes the slab used in the interferometer. For the calculations we have chosen in the plots a potential  $V = 54$  neV, as in the case of Si. In the experiment, one can use thick crystals because the absorption is low and the incoherent scattering is small. Note that materials such as iron are not suitable because they are magnetic.

- The geometry of the experimental setup and characteristics of the mirrors. The symmetric arrangement outlined in Fig. 1 is the simplest, but an asymmetric or a focusing design could also be analyzed. Such studies will be conducted in a future work. Other non-interferometric configurations could also be worth investigating, although a significant simplification of implementation would likely result in a lower sensitivity. A

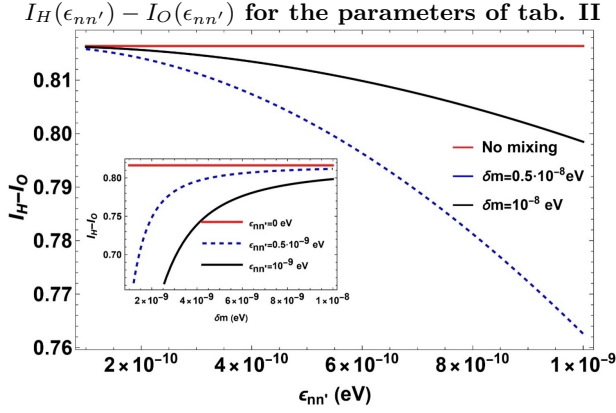
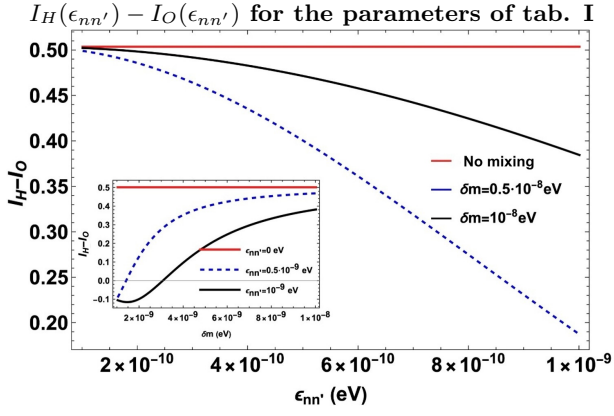


FIG. 4. Difference intensity  $I_H - I_O$  as a function of  $\epsilon_{nn'} \in [10^{-10}, 10^{-9}]$  eV for fixed values of  $\delta m$ . Red line: case without mixing, blue dotted line:  $\delta m = 0.5 \cdot 10^{-8}$  eV and black line:  $\delta m = 10^{-8}$  eV. The inset shows  $I_H - I_O$  as a function of  $\delta m \in [10^{-9}, 10^{-8}]$  eV for constant  $\epsilon_{nn'}$ . The red, blue dotted, and the black lines indicate the results for  $\epsilon_{nn'} = 0$  eV,  $\epsilon_{nn'} = 0.5 \cdot 10^{-9}$  eV, and  $\epsilon_{nn'} = 10^{-9}$  eV, respectively.

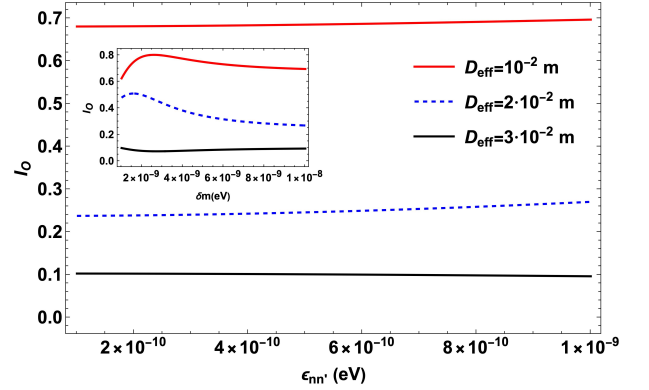
simple scenario could involve a counting experiment on a single arm, where the neutron beam is subject to a material potential (passing through a slab) and/or a magnetic field, measuring the decrease in intensity due to mixing. These ideas will be developed in future studies.

In all plots presented in this paper, the magnetic field  $\vec{B}_I$  has been fixed at zero thus allowing to vary the phase shift due to the field  $\vec{B}_{II}$  over a maximum range (see Fig. 1). Note that the phase difference between the beams along path I and II can also be changed by rotating the Si-block.

Figures 5 and 6 show, respectively, the behavior of  $I_O$  as a function of the effective phase shifter's length  $D_{eff}$  and the magnetic field  $B_{II}$ . These parameters can be controlled in the laboratory and allow for a systematic exploration of the interference pattern. By varying  $D_{eff}$  and  $B_{II}$ , these parameters can be adjusted in such a way that different regions of the parameter space can be explored. In particular, they can be set to reveal differences in the beam intensity depending on whether the oscillation is present or absent, thus providing a direct way to

test the presence of mirror neutrons in the experiment. The figures show that the relative changes in the intensities are more sensitive to changes in  $B_{II}$  than to  $\delta m$ .

$I_O(\epsilon_{nn'})$  for different values of  $D_{eff}$  and the parameters of tab. I



$I_O(\epsilon_{nn'})$  for different values of  $D_{eff}$  and the parameters of tab. II

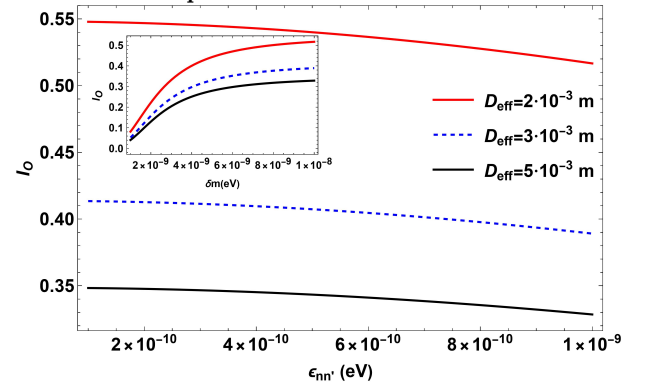


FIG. 5. Main graph: plot of the intensity  $I_O$  as a function of  $\epsilon_{nn'} \in [10^{-10}, 10^{-9}]$  eV for fixed values of  $\delta m = 10^{-8}$  eV and different values of  $D_{eff}$ . Inset: plot of  $I_O$  as a function of  $\delta m \in [10^{-9}, 10^{-8}]$  eV, for constant values of  $\epsilon_{nn'} = 10^{-9}$  eV and the same  $D_{eff}$  values used in the main plot.

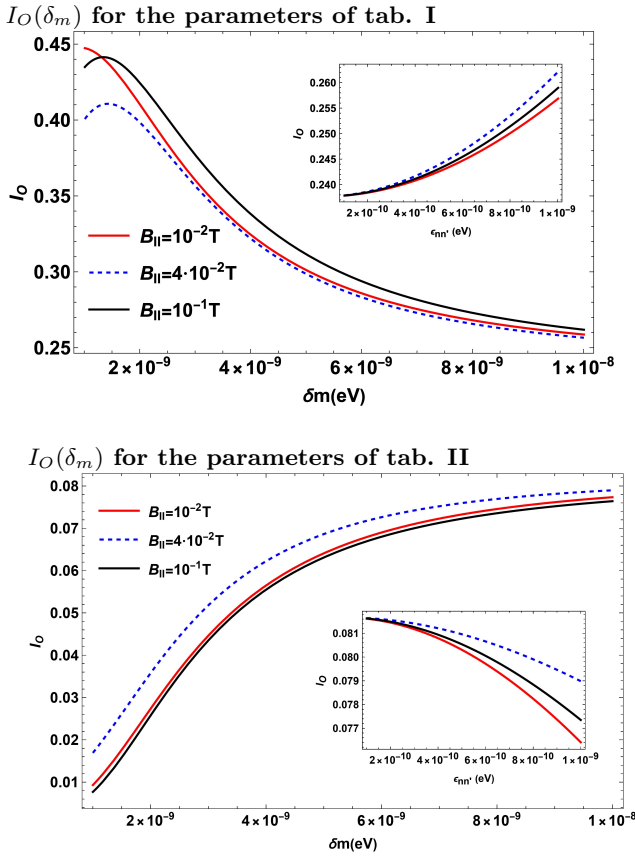


FIG. 6. Main graph: plot of the intensity  $I_O$  as a function of  $\delta_m \in [10^{-9}, 10^{-8}]$  eV for fixed values of  $\epsilon_{nn'} = 10^{-9}$  eV and different values of  $B_{II}$ . Inset: plot of  $I_O$  as a function of  $\epsilon_{nn'} \in [10^{-10}, 10^{-9}]$  eV, for constant values of  $\delta m = 10^{-8}$  eV and the same  $B_{II}$  values used in the main plot.

- *Gaussian wave packet:* - Until now, we have considered monochromatic plane waves. In order to increase the signal, one may use a beam with a bandwidth of the order  $\delta_B = 10\%$ . It corresponds to the typical spectrum used for small angle neutron scattering or reflectometry.  $\delta_B$  can be defined by means of a velocity selector or a bandpass multilayer. We consider a Gaussian wave packet, which for mathematical convenience is defined by discrete momentum values  $k_n = 2\pi n/a$ . The details are given in Appendix C. The evolution of the wave packet follows straightforwardly from the plane wave analysis performed above.

In the numerical analysis for the wave packet, we consider  $\lambda_0 = 8 \text{ \AA}$ ,  $a = 3200 \text{ \AA}$  and the parameters reported in Tables I and II. Fig. 7 shows the intensity  $I_O^G$ , for a wave packet, as a function of the parameter  $\epsilon_{nn'}$ , assuming  $\delta m$  to be fixed, and in the inset,  $I_O^G$  is shown versus  $\delta m$  for fixed  $\epsilon_{nn'}$ . The difference  $I_H^G - I_O^G$  as a function of  $\epsilon_{nn'}$ , for  $\delta m$  fixed is reported in Fig. 8 for different values of the spread in momentum  $\delta_B$ . The parameters considered in the numerical analysis are compatible with the theory of mirror matter, therefore, the above graphs show that the experimental setup presented here can probe a considerable range of neutron - mirror

neutron mixing parameters and allows the detection of mirror neutrons. The differences between the intensities  $I_H^G$  and  $I_O^G$  for the Gaussian wave packets are significantly reduced compared to the monochromatic case (Fig. 4). This reduction in signal contrast is attributed to the finite bandwidths  $\delta_B = 10\%$  and  $20\%$ , which cause a suppression of the interference fringes as contributions from different wavelengths average out.

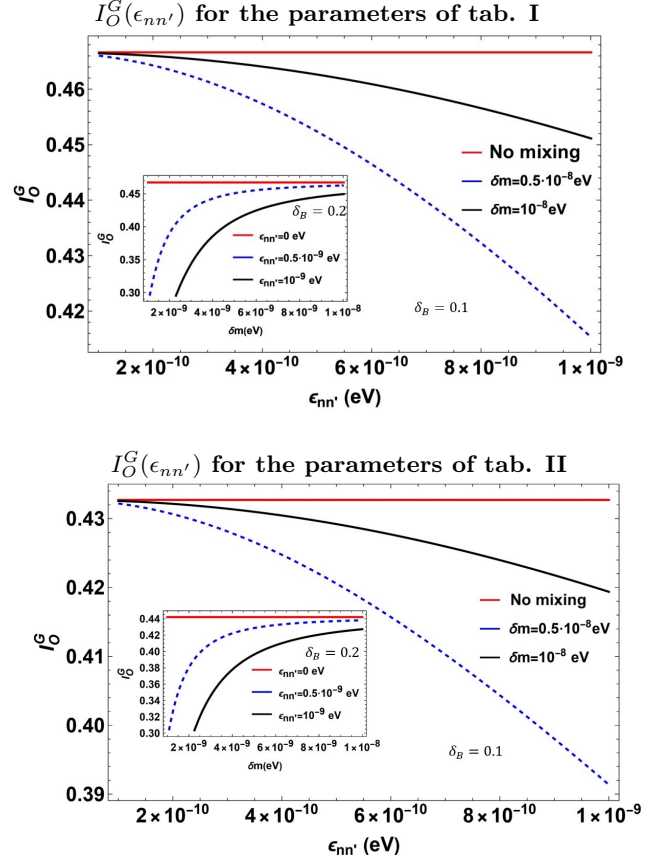


FIG. 7. Main graph: plot of the intensity  $I_O^G$  as a function of  $\epsilon_{nn'} \in [10^{-10}, 10^{-9}]$  eV for fixed values of  $\delta m$  and  $\delta_B = 0.1$ . Red line: case without mixing, blue dotted line:  $\delta m = 0.5 \cdot 10^{-8}$  eV, and black line:  $\delta m = 10^{-8}$  eV. Inset: plot of  $I_O^G$  as a function of  $\delta m \in [10^{-9}, 10^{-8}]$  eV, for constant values of  $\epsilon_{nn'}$  and  $\delta_B = 0.1$ . Red line:  $\epsilon_{nn'} = 0$  eV, blue dotted line:  $\epsilon_{nn'} = 10^{-10}$  eV, and black line:  $\epsilon_{nn'} = 10^{-9}$  eV.

- *Estimation of sensitivity:* - In the following we estimate the signal strength at the detectors of the interferometer. If the brilliance of the neutron source is known, the neutron intensity  $I$  entering the interferometer can be easily calculated [67]. It is given by:

$$I = A \cdot \Delta\lambda \cdot \Omega \cdot \Psi, \quad (9)$$

where  $A$ ,  $\Delta\lambda$ , and  $\Omega$  denote the beam size, wavelength band, and solid angle at the entrance of an experiment.  $\Psi$  is the brilliance of the neutron source. For example, the H15 neutron guide at the HFR of the Institute Laue-Langevin (ILL) delivers a brilliance of  $2.5 \cdot 10^{11} \text{ cm}^{-2} \text{ s}^{-1} \text{ \AA}^{-1} \text{ sr}^{-1}$  at  $\lambda = 8 \text{ \AA}$  [68].

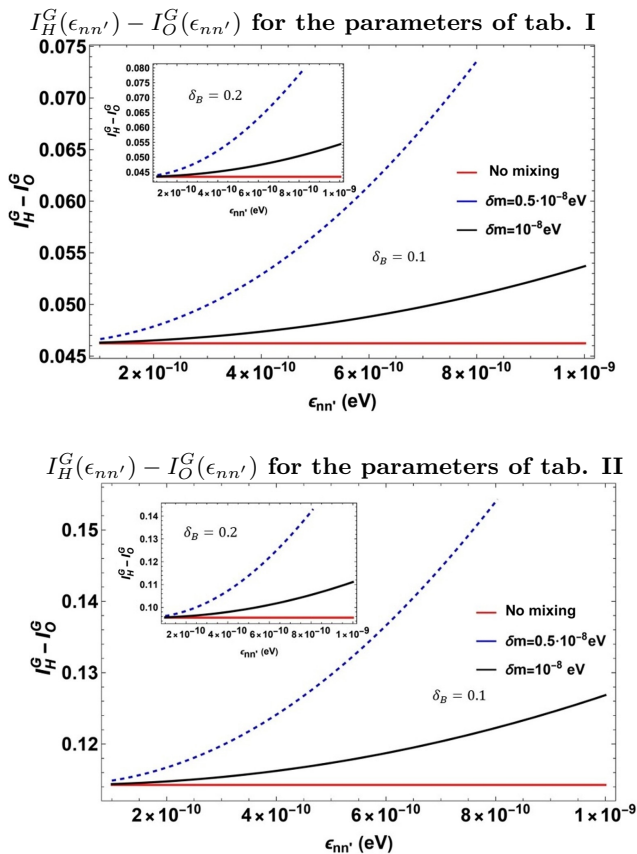


FIG. 8. Plot of the difference intensity  $I_H^G - I_O^G$  as a function of  $\epsilon_{nn'} \in [10^{-10}, 10^{-9}]$  eV for fixed values of  $\delta m$ . The main graph and the inset provide the results for  $\delta_B = 0.1$  and  $\delta_B = 0.2$ , respectively.

To obtain a rough estimate for the intensity at the detectors, we have adopted typical design parameters based on the work by Ebisawa et al. for a multilayer interferometer [60]. For example, we assumed a beam size  $0.5 \times 2.5$  mm<sup>2</sup>,  $\Delta\lambda = 0.24$  Å (corresponding to  $\delta B = 3\%$ ), and  $\Omega = 2.5 \cdot 10^{-6}$  sr. Additionally, we assumed that of every 100 neutrons striking the polarizer, 45 polarized neutrons would be reflected onto the beam splitter. The reflectivity of the bandpass mirrors was assumed to be 90%. Neglecting other losses, this results in an intensity of the order of 760 counts/s at the H and O detectors. Sources of error, leading to a reduction of the visibility, such as thermal noise, vibrational noise, gravity, waviness of the mirrors, mirror alignment, etc. can, of course, only be precisely quantified during the experimental procedure. Strategies for reducing such errors will be investigated in a separate experimental study. The experiment can be further improved by using position-sensitive detectors (PSDs), such as those used in MIEZE spectrometers [69]. PSDs allow for higher visibility because signal averaging due to interference fringes can be avoided. It may even be possible to increase the beam size and divergence of

the incident beam without reducing the sensitivity of the interferometer.

Assuming a signal strength of the order of 5% of the total intensity due to the mirror neutrons, the required statistics can be easily achieved within one hour of measurement. More precisely, up to  $2.7 \cdot 10^6 \pm 1700$  events are counted within one hour. The signal strength of the mirror neutrons is approximately 130'000 events, which is clearly distinguishable from the total measured intensity. Should it turn out that, for example, the beam size and/or the divergence of the incident beam need to be further reduced, sufficient leeway of several orders of magnitude is available for this purpose.

Finally, note that the absorption of neutrons by REC and BS affects the intensities by approximately 1.3% to 1.9% (see Appendix D), with uncertainty less than 0.1%. In contrast, neutron mixing with mirror neutrons affects the intensity of the beam by about 3%. Therefore, while an overall reduction in beam intensity of up to 2% percent can be explained by the absorption process by the mirrors, a decrease in total intensity of about 3% – 5% percent cannot be attributed to this phenomenon, but to the mixing effect. Therefore, the effects of the mixing, if it exists, are detectable with the analyzed interferometers.

- *Conclusions:* - We have explored the possibility of detecting mirror matter using neutron interferometry. We propose an experimental configuration that uses multilayers to separate, reflect, and combine the interfering neutron beams. Our calculations show that it should be possible to detect mirror matter for mixing amplitudes  $\epsilon_{nn'} \in [\simeq 2 \cdot 10^{-10}, 10^{-9}]$  eV and mass splittings  $\delta m \in [10^{-9}, 10^{-8}]$  eV if the interferometer is placed in a cold neutron beam of a reasonably powerful neutron source that is typically employing fission or spallation processes.

## ACKNOWLEDGMENTS

Partial financial support from MUR and INFN is acknowledged. A.C. also acknowledges the COST Action CA1511 Cosmology and Astrophysics Network for Theoretical Advances and Training Actions (CANTATA).

## Appendix A: Propagation of the beam, explicit computations

We consider a polarized neutron beam that propagates from the polarizing mirror to the beam splitter over a distance of length  $L_P$  before reaching it at time  $t = t_0$ . Assuming that the beam emerging from the polarizer at  $t = t_{-1}$  contains only neutrons, the initial state can be written as  $|\psi(t_{-1})\rangle = e^{i\phi} |n\rangle$ . The state at the beam splitter is then

$$\begin{aligned}
|\psi(L_P)\rangle &= e^{i\phi} \left[ \cos\theta(0,0)e^{-\frac{-iE_1(0,0)L_P}{v_n}} |n_1(0,0)\rangle + \sin\theta(0,0)e^{-\frac{-iE_2(0,0)L_P}{v_n}} |n_2(0,0)\rangle \right] \\
&= e^{i\phi} \left[ \cos\theta(0,0)e^{-\frac{-iE_1(0,0)L_P}{v_n}} (\cos\theta(0,0)|n\rangle - \sin\theta(0,0)|n'\rangle) \right. \\
&\quad \left. + \sin\theta(0,0)e^{-\frac{-iE_2(0,0)L_P}{v_n}} (\sin\theta(0,0)|n\rangle + \cos\theta(0,0)|n'\rangle) \right] \\
&= e^{i\phi} \left[ \cos^2\theta(0,0)e^{-\frac{-iE_1(0,0)L_P}{v_n}} + \sin^2\theta(0,0)e^{-\frac{-iE_2(0,0)L_P}{v_n}} \right] |n\rangle \\
&\quad + e^{i\phi} \cos\theta(0,0)\sin\theta(0,0) \left[ e^{-\frac{-iE_2(0,0)L_P}{v_n}} - e^{-\frac{-iE_1(0,0)L_P}{v_n}} \right] |n'\rangle, \tag{A1}
\end{aligned}$$

Here  $\theta(0,0)$ ,  $E_J(0,0)$ , and  $|n_i(0,0)\rangle$  denote the mixing angle, eigenenergies, and eigenstates evaluated for  $V = 0$  and  $B = 0$ , and the rotation defined by Eq. (5) (and its inverse) has been used.

At the beam splitter, the state can be expressed as

$$|\psi(0)\rangle = N_0 |n\rangle + M_0 |n'\rangle, \tag{A2}$$

where the coefficients are

$$N_0 = e^{i\phi} \left[ \cos^2\theta(0,0)e^{-\frac{-iE_1(0,0)L_P}{v_n}} + \sin^2\theta(0,0)e^{-\frac{-iE_2(0,0)L_P}{v_n}} \right], \tag{A3}$$

$$M_0 = e^{i\phi} \cos\theta(0,0)\sin\theta(0,0) \left[ e^{-\frac{-iE_2(0,0)L_P}{v_n}} - e^{-\frac{-iE_1(0,0)L_P}{v_n}} \right]. \tag{A4}$$

Beam I: We assume that the neutron beam impinges the beam splitter at  $t = 0$ . It is comprised only of a neutron component because the mirror part is not reflected by the *BS*. Let  $N_0^I$  and  $N_0^{II}$  denote the initial amplitudes for beam I and II. Note that any neutron absorption by *BS* is encoded within  $N_0^I$  and  $N_0^{II}$  that are given in terms of  $N_0$  and  $M_0$  as:

$$N_0^I = \sqrt{1 - A_{BS}R_{BS}} N_0 \tag{A5}$$

$$N_0^{II} = \sqrt{1 - A_{BS}T_{BS}} N_0 \tag{A6}$$

The initial state for beam I is therefore  $|\psi^I(0)\rangle = N_0^I |n\rangle$ . The beam traverses a region with a guide field  $B_g = 2$  mT and with zero potential of length  $l_1 = l$ .<sup>4</sup> From Eq.(5), we have the following state normalized to the initial amplitude:

$$\begin{aligned}
\frac{|\psi^I(l)\rangle}{N_0^I} &= \cos\theta(0,0)e^{-\frac{-iE_1(0,0)l}{v_n}} |n_1(0,0)\rangle + \sin\theta(0,0)e^{-\frac{-iE_2(0,0)l}{v_n}} |n_2(0,0)\rangle \\
&= \cos\theta(0,0)e^{-\frac{-iE_1(0,0)l}{v_n}} (\cos\theta(0,0)|n\rangle - \sin\theta(0,0)|n'\rangle) \\
&\quad + \sin\theta(0,0)e^{-\frac{-iE_2(0,0)l}{v_n}} (\sin\theta(0,0)|n\rangle + \cos\theta(0,0)|n'\rangle) \\
&= \left[ \cos^2\theta(0,0)e^{-\frac{-iE_1(0,0)l}{v_n}} + \sin^2\theta(0,0)e^{-\frac{-iE_2(0,0)l}{v_n}} \right] |n\rangle + \cos\theta(0,0)\sin\theta(0,0) \left[ e^{-\frac{-iE_2(0,0)l}{v_n}} - e^{-\frac{-iE_1(0,0)l}{v_n}} \right] |n'\rangle. \tag{A7}
\end{aligned}$$

We can read off the amplitudes at the entrance of the magnetic area as

$$N_1^I = N_0^I \left[ \cos^2\theta(0,0)e^{-\frac{-iE_1(0,0)l}{v_n}} + \sin^2\theta(0,0)e^{-\frac{-iE_2(0,0)l}{v_n}} \right] \tag{A8}$$

$$M_1^I = N_0^I \cos\theta(0,0)\sin\theta(0,0) \left[ e^{-\frac{-iE_2(0,0)l}{v_n}} - e^{-\frac{-iE_1(0,0)l}{v_n}} \right]. \tag{A9}$$

Beam I does then traverse the area filled with magnetic field  $B_I$  for a distance  $l_2 = L$ , up to the central mirror  $C_I$ . The state at the entrance is now  $|\psi_1^I\rangle = N_1^I |n\rangle + M_1^I |n'\rangle$ . We proceed in the same way as before, just we have to consider the presence of the magnetic field  $B_I$ . Since the mirror neutron component is entirely transmitted by the

<sup>4</sup> We point out that both beam paths are exposed to  $B_g = 2$  mT,

thus the phase shift due to  $B_g$  is canceled.

mirror  $C_I$ , the state after reflection from  $C_I$  is of the form  $R_C^I N_2^I |n\rangle$ . At the distance  $L$ , immediately before  $C_I$ , the neutron and mirror-neutron states are (note that now  $V = 0$  and  $B = B_I$ ):

$$\begin{aligned}
|n\rangle &\rightarrow \cos\theta(0, B_I) e^{\frac{-iE_1(0, B_I)L}{v_n}} |n_1(0, B_I)\rangle + \sin\theta(0, B_I) e^{\frac{-iE_2(0, B_I)L}{v_n}} |n_2(0, B_I)\rangle \\
&= \cos\theta(0, B_I) e^{\frac{-iE_1(0, B_I)L}{v_n}} (\cos\theta(0, B_I) |n\rangle - \sin\theta(0, B_I) |n'\rangle) \\
&+ \sin\theta(0, B_I) e^{\frac{-iE_2(0, B_I)L}{v_n}} (\sin\theta(0, B_I) |n\rangle + \cos\theta(0, B_I) |n'\rangle) \\
&= \left[ \cos^2\theta(0, B_I) e^{\frac{-iE_1(0, B_I)L}{v_n}} + \sin^2\theta(0, B_I) e^{\frac{-iE_2(0, B_I)L}{v_n}} \right] |n\rangle \\
&+ \cos\theta(0, B_I) \sin\theta(0, B_I) \left[ e^{\frac{-iE_2(0, B_I)L}{v_n}} - e^{\frac{-iE_1(0, B_I)L}{v_n}} \right] |n'\rangle
\end{aligned}$$

and

$$\begin{aligned}
|n'\rangle &\rightarrow \cos\theta(0, B_I) e^{\frac{-iE_2(0, B_I)L}{v_n}} |n_2(0, B_I)\rangle - \sin\theta(0, B_I) e^{\frac{-iE_1(0, B_I)L}{v_n}} |n_1(0, B_I)\rangle \\
&= \cos\theta(0, B_I) e^{\frac{-iE_2(0, B_I)L}{v_n}} (\cos\theta(0, B_I) |n'\rangle + \sin\theta(0, B_I) |n\rangle) \\
&- \sin\theta(0, B_I) e^{\frac{-iE_1(0, B_I)L}{v_n}} (-\sin\theta(0, B_I) |n'\rangle + \cos\theta(0, B_I) |n\rangle) \\
&= \left[ \cos^2\theta(0, B_I) e^{\frac{-iE_2(0, B_I)L}{v_n}} + \sin^2\theta(0, B_I) e^{\frac{-iE_1(0, B_I)L}{v_n}} \right] |n'\rangle \\
&+ \cos\theta(0, B_I) \sin\theta(0, B_I) \left[ e^{\frac{-iE_2(0, B_I)L}{v_n}} - e^{\frac{-iE_1(0, B_I)L}{v_n}} \right] |n\rangle,
\end{aligned}$$

respectively, so that we have

$$\begin{aligned}
N_2^I &= N_1^I \left[ \cos^2\theta(0, B_I) e^{\frac{-iE_1(0, B_I)L}{v_n}} + \sin^2\theta(0, B_I) e^{\frac{-iE_2(0, B_I)L}{v_n}} \right] \\
&+ M_1^I \cos\theta(0, B_I) \sin\theta(0, B_I) \left[ e^{\frac{-iE_2(0, B_I)L}{v_n}} - e^{\frac{-iE_1(0, B_I)L}{v_n}} \right]
\end{aligned} \tag{A10}$$

and the state, immediately after  $C_I$  is just  $|\psi_2^I\rangle = R_C^I N_2^I |n\rangle$ . We now iterate the same process for another length  $L$ . From now on the relations among the intermediate amplitudes shall be omitted and reported in the appendix B. At the exit of the magnetic area the state is  $|\psi_3^I\rangle = N_3^I |n\rangle + M_3^I |n'\rangle$ . The beam traverses another field region with  $B_g = 2$  mT of a length  $l_4 = l$ , thus, after the recombination mirror, one has  $|\psi_{4H}^I\rangle = \sqrt{1 - A_{REC}} R_{REC} N_4^I |n\rangle$  and  $|\psi_{4O}^I\rangle = \sqrt{1 - A_{REC}} T_{REC} M_4^I |n\rangle + M_4^I |n'\rangle$ , respectively, directed towards the H and O detector.

## Appendix B: Relations among intermediate amplitudes and transmission and reflection coefficients

Here, we provide explicitly all the intermediate amplitudes. For the beam I:

$$\begin{aligned}
N_3^I &= R_C^I N_2^I \left[ \cos^2\theta(0, B_I) e^{\frac{-iE_1(0, B_I)L}{v_n}} + \sin^2\theta(0, B_I) e^{\frac{-iE_2(0, B_I)L}{v_n}} \right] \\
M_3^I &= R_C^I N_2^I \cos\theta(0, B_I) \sin\theta(0, B_I) \left[ e^{\frac{-iE_2(0, B_I)L}{v_n}} - e^{\frac{-iE_1(0, B_I)L}{v_n}} \right]
\end{aligned} \tag{B1}$$

$$\begin{aligned}
N_4^I &= N_3^I \left[ \cos^2\theta(0, 0) e^{\frac{-iE_1(0, 0)l}{v_n}} + \sin^2\theta(0, 0) e^{\frac{-iE_2(0, 0)l}{v_n}} \right] + M_3^I \cos\theta(0, 0) \sin\theta(0, 0) \left[ e^{\frac{-iE_2(0, 0)l}{v_n}} - e^{\frac{-iE_1(0, 0)l}{v_n}} \right] \\
M_4^I &= M_3^I \left[ \cos^2\theta(0, 0) e^{\frac{-iE_2(0, 0)l}{v_n}} + \sin^2\theta(0, 0) e^{\frac{-iE_1(0, 0)l}{v_n}} \right] + N_3^I \cos\theta(0, 0) \sin\theta(0, 0) \left[ e^{\frac{-iE_2(0, 0)l}{v_n}} - e^{\frac{-iE_1(0, 0)l}{v_n}} \right]
\end{aligned} \tag{B2}$$

For the beam II, the free evolution on the length  $l'$  is characterized by

$$\begin{aligned}
N_1^{II} &= N_0^{II} \left[ \cos^2\theta(0, 0) e^{\frac{-iE_1(0, 0)l'}{v_n}} + \sin^2\theta(0, 0) e^{\frac{-iE_2(0, 0)l'}{v_n}} \right] \\
&+ M_0 \cos\theta(0, 0) \sin\theta(0, 0) \left[ e^{\frac{-iE_2(0, 0)l'}{v_n}} - e^{\frac{-iE_1(0, 0)l'}{v_n}} \right] \\
M_1^{II} &= N_0^{II} \cos\theta(0, 0) \sin\theta(0, 0) \left[ e^{\frac{-iE_2(0, 0)l'}{v_n}} - e^{\frac{-iE_1(0, 0)l'}{v_n}} \right] \\
&+ M_0 \left[ \cos^2\theta(0, 0) e^{\frac{-iE_2(0, 0)l'}{v_n}} + \sin^2\theta(0, 0) e^{\frac{-iE_1(0, 0)l'}{v_n}} \right].
\end{aligned} \tag{B3}$$

The evolution within the slab, considering the modified speed  $v_n(V)$ , gives the following amplitudes right after the slab:

$$\begin{aligned}
N_2^{II} &= N_1^{II} \left[ \cos^2 \theta(V, 0) e^{\frac{-iE_1(V, 0)D_{eff}}{v_n(V)}} + \sin^2 \theta(V, 0) e^{\frac{-iE_2(V, 0)D_{eff}}{v_n(V)}} \right] \\
&+ M_1^{II} \cos \theta(V, 0) \sin \theta(V, 0) \left[ e^{\frac{-iE_2(V, 0)D_{eff}}{v_n(V)}} - e^{\frac{-iE_1(V, 0)D_{eff}}{v_n(V)}} \right] \\
M_2^{II} &= M_1^{II} \left[ \cos^2 \theta(V, 0) e^{\frac{-iE_2(V, 0)D_{eff}}{v_n(V)}} + \sin^2 \theta(V, 0) e^{\frac{-iE_1(V, 0)D_{eff}}{v_n(V)}} \right] \\
&+ N_1^{II} \cos \theta(V, 0) \sin \theta(V, 0) \left[ e^{\frac{-iE_2(V, 0)D_{eff}}{v_n(V)}} - e^{\frac{-iE_1(V, 0)D_{eff}}{v_n(V)}} \right].
\end{aligned} \tag{B4}$$

After the slab, the beam traverse again a free region of length  $l''$  ( $l' + l'' + D_{eff} = d_1$ ). At the entrance of the magnetic area the amplitudes are

$$\begin{aligned}
N_3^{II} &= N_2^{II} \left[ \cos^2 \theta(0, 0) e^{\frac{-iE_1(0, 0)l''}{v_n}} + \sin^2 \theta(0, 0) e^{\frac{-iE_2(0, 0)l''}{v_n}} \right] + M_2^{II} \cos \theta(0, 0) \sin \theta(0, 0) \left[ e^{\frac{-iE_2(0, 0)l''}{v_n}} - e^{\frac{-iE_1(0, 0)l''}{v_n}} \right] \\
M_3^{II} &= M_2^{II} \left[ \cos^2 \theta(0, 0) e^{\frac{-iE_2(0, 0)l''}{v_n}} + \sin^2 \theta(0, 0) e^{\frac{-iE_1(0, 0)l''}{v_n}} \right] + N_2^{II} \cos \theta(0, 0) \sin \theta(0, 0) \left[ e^{\frac{-iE_2(0, 0)l''}{v_n}} - e^{\frac{-iE_1(0, 0)l''}{v_n}} \right].
\end{aligned}$$

The neutron amplitude at  $C_{II}$  is

$$\begin{aligned}
N_4^{II} &= N_3^{II} \left[ \cos^2 \theta(0, B_{II}) e^{\frac{-iE_1(0, B_{II})L}{v_n}} + \sin^2 \theta(0, B_{II}) e^{\frac{-iE_2(0, B_{II})L}{v_n}} \right] \\
&+ M_3^{II} \cos \theta(0, B_{II}) \sin \theta(0, B_{II}) \left[ e^{\frac{-iE_2(0, B_{II})L}{v_n}} - e^{\frac{-iE_1(0, B_{II})L}{v_n}} \right]
\end{aligned} \tag{B5}$$

and immediately after, one has  $|\psi_{II}\rangle = R_C^{II} N^{II} |n\rangle$  since the mirror part has been fully transmitted. At the exit of the magnetic area we have

$$\begin{aligned}
N_5^{II} &= R_C^{II} N_4^{II} \left[ \cos^2 \theta(0, B_{II}) e^{\frac{-iE_1(0, B_{II})L}{v_n}} - \sin^2 \theta(0, B_{II}) e^{\frac{-iE_2(0, B_{II})L}{v_n}} \right] \\
M_5^{II} &= R_C^{II} N_4^{II} \cos \theta(0, B_{II}) \sin \theta(0, B_{II}) \left[ e^{\frac{-iE_2(0, B_{II})L}{v_n}} - e^{\frac{-iE_1(0, B_{II})L}{v_n}} \right].
\end{aligned} \tag{B6}$$

Finally

$$\begin{aligned}
N_6^{II} &= N_5^{II} \left[ \cos^2 \theta(0, 0) e^{\frac{-iE_1(0, 0)l}{v_n}} + \sin^2 \theta(0, 0) e^{\frac{-iE_2(0, 0)l}{v_n}} \right] + M_5^{II} \cos \theta(0, 0) \sin \theta(0, 0) \left[ e^{\frac{-iE_2(0, 0)l}{v_n}} - e^{\frac{-iE_1(0, 0)l}{v_n}} \right] \\
M_6^{II} &= M_5^{II} \left[ \cos^2 \theta(0, 0) e^{\frac{-iE_2(0, 0)l}{v_n}} + \sin^2 \theta(0, 0) e^{\frac{-iE_1(0, 0)l}{v_n}} \right] + N_5^{II} \cos \theta(0, 0) \sin \theta(0, 0) \left[ e^{\frac{-iE_2(0, 0)l}{v_n}} - e^{\frac{-iE_1(0, 0)l}{v_n}} \right].
\end{aligned} \tag{B7}$$

The amplitudes at the detectors are:

$$\begin{aligned}
N_H^I &= \sqrt{1 - A_{REC} R_{REC}} N_4^I \left[ \cos^2 \theta(0, 0) e^{\frac{-iE_1(0, 0)d}{v_n}} + \sin^2 \theta(0, 0) e^{\frac{-iE_2(0, 0)d}{v_n}} \right] \\
N_H^{II} &= \sqrt{1 - A_{REC} T_{REC}} N_6^{II} \left[ \cos^2 \theta(0, 0) e^{\frac{-iE_1(0, 0)d}{v_n}} + \sin^2 \theta(0, 0) e^{\frac{-iE_2(0, 0)d}{v_n}} \right] \\
&+ M_6^{II} \cos \theta(0, 0) \sin \theta(0, 0) \left[ e^{\frac{-iE_2(0, 0)d}{v_n}} - e^{\frac{-iE_1(0, 0)d}{v_n}} \right] \\
N_O^I &= \sqrt{1 - A_{REC} T_{REC}} N_4^I \left[ \cos^2 \theta(0, 0) e^{\frac{-iE_1(0, 0)d}{v_n}} + \sin^2 \theta(0, 0) e^{\frac{-iE_2(0, 0)d}{v_n}} \right] \\
&+ M_4^I \cos \theta(0, 0) \sin \theta(0, 0) \left[ e^{\frac{-iE_2(0, 0)d}{v_n}} - e^{\frac{-iE_1(0, 0)d}{v_n}} \right] \\
N_O^{II} &= \sqrt{1 - A_{REC} R_{REC}} N_6^{II} \left[ \cos^2 \theta(0, 0) e^{\frac{-iE_1(0, 0)d}{v_n}} + \sin^2 \theta(0, 0) e^{\frac{-iE_2(0, 0)d}{v_n}} \right].
\end{aligned} \tag{B8}$$

We set the transmission and reflection coefficients as follows:

$$\begin{aligned}
T_{BS}(\Gamma_{REC}, \varphi_{T_{BS}}) &= \sin(\Gamma_{BS}) e^{-i\varphi_{T_{BS}}}, & R_{BS}\left(\Gamma_{BS}, \varphi_{R_{BS}} = \frac{\pi}{2}\right) &= \cos(\Gamma_{BS}) e^{-i\frac{\pi}{2}}, \\
T_C^I(\Gamma_{R_C^I}, \varphi_{T_C^I}) &= \sin(\Gamma_{R_C^I}) e^{-i\varphi_{T_C^I}}, & R_C^I\left(\Gamma_{R_C^I}, \varphi_{R_C^I} = \frac{\pi}{2}\right) &= \cos(\Gamma_{R_C^I}) e^{-i\frac{\pi}{2}}, \\
T_C^{II}(\Gamma_{R_C^{II}}, \varphi_{T_C^{II}}) &= \sin(\Gamma_{R_C^{II}}) e^{-i\varphi_{T_C^{II}}}, & R_C^{II}\left(\Gamma_{R_C^{II}}, \varphi_{R_C^{II}} = \frac{\pi}{2}\right) &= \cos(\Gamma_{R_C^{II}}) e^{-i\frac{\pi}{2}}, \\
T_{REC}(\Gamma_{REC}, \varphi_{T_{REC}}) &= \sin(\Gamma_{REC}) e^{-i\varphi_{T_{REC}}}, & R_{REC}\left(\Gamma_{REC}, \varphi_{R_{REC}} = \frac{\pi}{2}\right) &= \cos(\Gamma_{REC}) e^{-i\frac{\pi}{2}}.
\end{aligned} \tag{B9}$$

Note that the absorption coefficients in the central mirrors  $A_C^I$ , and  $A_C^{II}$  are contained in the transmission coefficients  $T_C^I$  and  $T_C^{II}$ , which quantify the fraction of neutrons that are not reflected. It is worth noting that we assigned a phase shift of  $\pi/2$  to the reflection coefficients in Tables I and II. This phase relation is required to strictly satisfy the conservation of particle number. As discussed by Zeilinger [58], the condition  $|T|^2 + |R|^2 = 1$  is not sufficient to guarantee unitarity; for each mirror, the interference cross-terms must also vanish, satisfying the relation  $RT^* + TR^* = 0$ . We applied this specific phase difference to ensure that the final intensities derived in Eq. (8) satisfy the conservation condition  $I_O + I_H \leq 1$  (in terms of the initial amplitude).

### Appendix C: Gaussian wave packet

We take the initial state  $|\psi^I(0)\rangle$  as a Gaussian wave packet, which, for mathematical convenience, we consider discrete and centered at the wave vector  $k_0 = 2\pi/\lambda_0$  of the neutrons.<sup>5</sup>

$$|\psi^I(0)\rangle = \left( \sum_{m=1}^{\infty} e^{-\frac{(k_m - k_0)^2}{2\sigma_k^2}} \right)^{-1/2} \sum_{n=1}^{\infty} e^{-\frac{(k_n - k_0)^2}{4\sigma_k^2}} |\psi_{k_n}^I(0)\rangle.$$

Here, the wave vectors are given by  $k_n = \frac{2\pi n}{a}$ , with a finite lattice spacing  $a$ ,  $\sigma_k$  is the standard deviation in  $k$ -space, which can be parameterized as  $\sigma_k \simeq \delta_B k_0$ , where  $k_0$  is the central value of the Gaussian wave packet, and  $\delta_B$  is the fractional spread in momentum around  $k_0$ . Note that in the sum,  $n$  assumes only positive values, because we are interested in wave packets propagating in the forward direction. In practice, the range of  $n$ -values can be restricted so that only wave vectors  $k_n \simeq k_0$  are included that provide meaningful contributions to the sums. We assume that the reflection and transmission of the mirrors are only weakly dependent on the momentum of the neutrons in the range considered. Carrying out calculations similar to the ones performed for the monochromatic case, we obtain the following normalized intensities  $I_O$  and  $I_H$ :

$$I_O^G = \left( \sum_{m=1}^{\infty} e^{-\frac{(k_m - k_0)^2}{2\sigma_k^2}} \right)^{-2} \sum_{n=1}^{\infty} e^{-\frac{(k_n - k_0)^2}{2\sigma_k^2}} I_O(k_n), \quad I_H^G = \left( \sum_{m=1}^{\infty} e^{-\frac{(k_m - k_0)^2}{2\sigma_k^2}} \right)^{-2} \sum_{n=1}^{\infty} e^{-\frac{(k_n - k_0)^2}{2\sigma_k^2}} I_H(k_n),$$

where  $I_O(k_n)$  and  $I_H(k_n)$  denote the normalized intensities at  $O$  and  $H$  for a plane wave with momentum  $k_n$ .

### Appendix D: Absorption of reflecting mirrors

The sequence of the layer thicknesses of the Ni and Ti layers comprising the bandpass mirrors with a bandwidth of 10% has been extracted from the sequence of layers for supermirror as derived by Hayter and Mook [59]. For the half-transparent ( $ht$ ) mirrors (BS, REC) and the reflecting ( $r$ ) mirrors ( $C_I$ ,  $C_{II}$ ), the design reflectivity was set to  $R_{ht} = 48.5\%$  and  $R_r = 97.0\%$ , resulting in  $N_{ht} = 356$  and  $N_r = 2068$  single layers of Ni and Ti, respectively. The total thickness of the Ni- and Ti-layers for the half-transparent mirrors is  $0.435 \mu\text{m}$  and  $0.428 \mu\text{m}$ , respectively. The corresponding thicknesses for the reflecting mirrors are  $2.50 \mu\text{m}$  and  $2.46 \mu\text{m}$ , respectively. The reflection angle of

<sup>5</sup> In the expression for  $|\psi^I(0)\rangle$  one should in principle consider an integral instead of a summation; the discretization is introduced for numerical convenience, as the integral cannot be performed

analytically. The continuum may be recovered in the  $a \rightarrow 0$  limit. In any case, this approximation deviates negligibly from the exact result, as can be numerically verified.

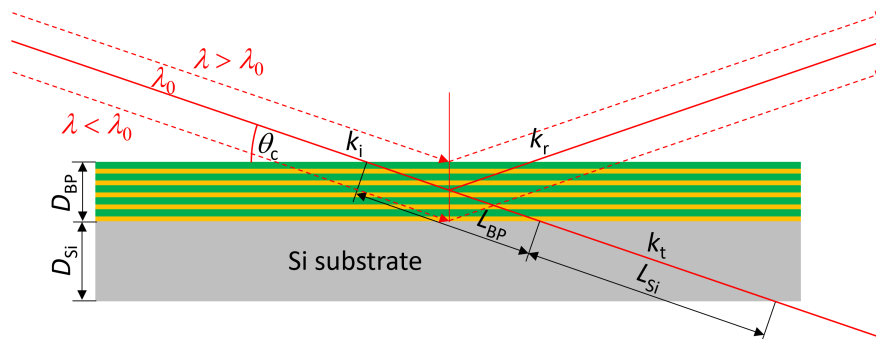


FIG. 9. The Ni/Ti layers of the bandpass mirrors are deposited on a Si substrate. The  $d$ -spacing of the Ni/Ti bilayers varies between  $45.6 \leq d \leq 50.8 \text{ \AA}$ . The transmitted rays pass through both the mirror layers and the Si substrate, while the reflected rays pass through the Ni/Ti layers twice. For reflection, the number of layers relevant for absorption depends on the wavelength of the neutrons.

neutrons with  $\lambda_0 = 8 \text{ \AA}$  amounts to  $\theta_c = 0.099 \cdot 6 \cdot 8 = 4.8^0$ . Therefore, neglecting refraction at the interfaces air - mirror, mirror - substrate, and substrate - air, the path lengths in the bandpass mirrors and the substrates are given by  $L_{BP} = D_{BP}/\sin(\theta_c)$  and  $L_{Si} = D_{Si}/\sin(\theta_c)$ , respectively (Fig. 9).

The half-transparent mirrors for BS and REC are coated on Si-wafer with a thickness of 0.3 mm. Using *measured* absorption values of Ni and Ti, which include also the incoherent scattering (and agree with the *calculated* values), one obtains a transmission of the mirrors of  $T_{ht} = 98.1\%$ . The absorption is essentially caused by the Si-wafer. For the reflecting mirrors we assume that the neutrons pass the mirror structure in average approximately once. The reason being that according to Fig. 9, neutrons with  $\lambda > \lambda_0$  are predominantly reflected from the upper layers only while the neutrons with  $\lambda < \lambda_0$  are reflected from the bottom layers. The thin layers of multilayers are usually deposited first because they are more sensitive to the effects of roughness. As a result, the intensity of the reflected beam ends up to be 98.7% of the incident beam. In practice, the reflectivity of the mirrors  $C_I$  and  $C_{II}$  is of the order of  $R_r \simeq 88\%$ . Therefore, the effects of absorption, which affect the intensities by approximately 1.3% to 1.9% can be safely neglected. The absorption in the BS and REC mirrors could be partially compensated by increasing the design reflectivity from  $R_{ht} = 48.5\%$  to  $R_{ht} = 50.4\%$ .

- 
- [1] V. Trimble, Annual Review of Astronomy and Astrophysics, **25**, 425-472, (1987).
  - [2] P. J. E. Peebles and B. Ratra, Reviews of modern physics, **75**, 559, (2003).
  - [3] M. Li, Xiao-Dong Li, S. Wang and Yi Wang, Frontiers of Physics, **8**, 828-846, (2013).
  - [4] Dark Energy Survey Collaboration: T. Abbott, F. B. Abdalla, J. Aleksić, S. Allam, A. Amara, D. Bacon, E. Balbinot, M. Banerji, K. Bechtol et al, Monthly Notices of the Royal Astronomical Society, **460**, 1270-1299, (2016).
  - [5] G. Bertone and D. Hooper, Rev. Mod. Phys., **90**, 045002, (2018).
  - [6] F. Zwicky, The Astrophysical Journal. **86**: 217–246, (1937).
  - [7] V.C. Rubin, W.K. Jr. Ford, The Astrophysical Journal. **159**: 379–403, (1970).
  - [8] S. Profumo, L. Giani and O. F. Piattella, Universe, **5**, 213, (2019).
  - [9] P. Salucci et al., Frontiers in Physics, **8**, (2020).
  - [10] A. Arbey and F. Mahmoudi, Progress in Particle and Nuclear Physics, **119**, 103865, (2021).
  - [11] J. E. Kim and G. Carosi, Reviews of Modern Physics, **82**, 557–601, (2010).
  - [12] R.D. Peccei, H.R. Quinn, Physical Review Letters. **38** (25): 1440–1443, (1977). R. D. Peccei, Adv. Ser. Direct. High Energy Phys, **3**, 503, (1989).
  - [13] M. Dine and N. Seiberg, Nuclear Physics B, **273**, 109-124, (1986).
  - [14] S. M. Bilenky and B. Pontecorvo, Physics Reports, **41**, 225-261, (1978).
  - [15] S. M. Bilenky and S. T. Petcov, Reviews of Modern Physics, **59**, 671, (1987).
  - [16] M. Blasono, A. Capolupo and G. Vitiello, Physical Review D, **66**, 025033, (2002).
  - [17] T. Kajita, Reports on Progress in Physics, **69**, 1607, (2006).
  - [18] A. Capolupo, G. Lambiase, and A. Quaranta, Physical Review D, **101**, 095022, (2020).
  - [19] S. P. Mikheyev and A. Y. Smirnov, Progress in Particle and Nuclear Physics, **23**, 41-136, (1989).
  - [20] E. Akhmedov, A. Y. Smirnov, Journal of High Energy Physics, **2022**, 1-21, (2022).
  - [21] A. Capolupo, S. M. Giampaolo, A. Quaranta, Physics Letters B, **820**, 136489, (2021).

- [22] S. M. Bilenky, J. Hošek and S. T. Petcov, *Physics Letters B*, **94**, 495-498, (1980).
- [23] A. Capolupo, S. M. Giampaolo, B. C. Hiesmayr, G. Lambiase, and A. Quaranta, *Journal of Physics G: Nuclear and Particle Physics*, **50**, 025001, (2023).
- [24] M. Beuthe, *Physical Review D*, **66**, 013003, (2002).
- [25] A. Capolupo, and A. Quaranta, *Journal of Physics G: Nuclear and Particle Physics*, **50**, 055003, (2023).
- [26] A. Capolupo and A. Quaranta, *Physics Letters B*, 137776, (2023).
- [27] D. Barducci, and C. Toni, *Journal of High Energy Physics*, **2023**, 1–46, (2023).
- [28] J. L. Feng, B. Fornal, I. Galon, S. Gardner, J. Smolinsky, T. M. P. Tait, and P. Tanedo, *Physical Review D*, **95**, 035017, (2017).
- [29] A. Capolupo, A. Quaranta, R. Serao, *Physics of the Dark Universe*, **47**, 101748, (2025).
- [30] A. Capolupo, G. Lambiase, and A. Quaranta, *Physics Letters B*, **829**, 137128, (2022).
- [31] D. Huang, A. P. Morais and R. Santos, *Physical Review D*, **102**, 075009, (2020).
- [32] J. Cao, L. Meng, L. Shang, S. Wang and B. Yang, *Physical Review D*, **106**, 055042, (2022).
- [33] J. Bordes, Hong-Mo Chan, and S. T. Tsou, *International Journal of Modern Physics A*, **34**, 1950140, (2019).
- [34] F. Chadha-Day, J. Ellis and D. J.E. Marsh, *Science advances*, **8**, eabj3618, (2022).
- [35] C. Bartram et al., *Physical review letters*, **127**, 261803, (2021).
- [36] I. De Martino, T. Broadhurst, S. H. H. Tye, T. Chiueh, Hsi-Yu Schive and R. Lazkoz, *Galaxies*, **6**, 10, (2018).
- [37] I. De Martino, *Physical Review D*, **108**, 123044, (2023).
- [38] A. Capolupo, I. De Martino, G. Lambiase and A. Stabile, *Physics Letters B*, **790**, 427-435, (2019).
- [39] A. Capolupo, G. Lambiase, A. Quaranta, S. M. Giampaolo, *Physics Letters B*, **804**, 135407, (2020).
- [40] A. Capolupo, S. M. Giampaolo and A. Quaranta, *The European Physical Journal C*, **81**, 1116, (2021).
- [41] A. Capolupo, *Advances in High Energy Physics*, 8089142, (2016).
- [42] A. Capolupo, A. Quaranta and R. Serao, *Symmetry*, 807, (2023).
- [43] A. Capolupo, *Advances in High Energy Physics*, 9840351, (2018).
- [44] A. Capolupo, S. Carloni and A. Quaranta, *Phys. Rev. D*, 105013, (2022).
- [45] A. Capolupo, S. M. Giampaolo, G. Lambiase and A. Quaranta, *Eur. Phys. J. C*, 423, (2020).
- [46] A. Capolupo, S. Capozziello, G. Pisacane and A. Quaranta, *Phys. Dark Univ.*, 101894, (2025).
- [47] Z. Berezhiani, *Eur. Phys. J. C*, 484, (2019).
- [48] A. Capolupo, G. Pisacane, A. Quaranta and F. Romeo, *Phys. Dark Univ.*, 101688, (2024).
- [49] D. Zhou, *Universe*, 484, (2023).
- [50] I. Yu. Kobzarev, L. B. Okun, and I. Ya. Pomeranchuk, *Sov. J. Nucl. Phys.*, 837–841, (1966).
- [51] S. I. Blinnikov, and M. Yu. Khlopov, *Sov. J. Nucl. Phys.*, 472, (1982).
- [52] Z. Berezhiani, *Int. J. Mod. Phys. A*, **19**, 3775–3806, (2004).
- [53] H. M. Hodges, *Phys. Rev. D*, **47**, 456–459, (1993).
- [54] R. Foot, *Int. J. Mod. Phys. A*, **29**, 1430013, (2014).
- [55] M. Hostert, D. McKeen, M. Pospelov, and N. Raj, *Phys. Rev. D*, **107**, 075034, (2023).
- [56] Y. Hao and D. Ni, *Phys. Rev. D*, **106**, 115028, (2022).
- [57] H. Rauch, W. Treimer and U. Bonse, *Physics Letters A*, **47**, 369-371, (1974).
- [58] A. Zeilinger, *Am. J. Phys.* **49**, 882 (1981).
- [59] J. B. Hayter and H. A. Mook, *J. Appl. Cryst.*, **22**, 35-41, (1989).
- [60] T. Ebisawa et al., *NIM-A*, **344**, 597-606. (1994)
- [61] V. F. Sears, *Neutron News* **3**, 26–37 (1992).
- [62] M. Janoschek, S. Klimko, R. Gähler, B. Roessli, and P. Böni, *Spherical neutron polarimetry with mupad*, *Phys. B: Condens. Matter*, **397**, 125 (2007).
- [63] H. Lemmel and A. G. Wagh, *Phys. Rev. A*, **82**, 033626, (2010).
- [64] C. Schanzer, M. Schneider, P. Böni, *Journal of Physics: Conference Series*, **746**, IOP Publishing, 012024, (2016).
- [65] R. Kolevatorov, C. Schanzer, P. Böni, *Nuc. Inst. Meth. Phys. Res.*, **922**, 98-107, (2019)
- [66] O. Zimmer et al., *Jadavpur Journal of International Relations*, **24**, 95-110, (2022).
- [67] P. Böni, *J. Phys.: Conf. Ser.* **502** 012047 (1-6), (2014).
- [68] *Yellow Book of the ILL 1986*, p 8, Fig. 4.
- [69] C. Franz, O. Soltwedel, C. Fuchs, S. Säubert, F. Haslbeck, A. Wendl, J.K. Jochum, P. Böni, and C. Pfeifferer, *Nuc. Inst. Meth. Phys. Res.*, **939**, 22-29, (2019).